

Control of a Satellite Formation For Imaging Applications

Islam I. Hussein¹

Daniel J. Scheeres²

David C. Hyland³

Abstract

In this paper we state the basic governing relationships between a constellation's motion in physical two dimensional space and imaging objectives. We then introduce a class of motions that satisfies imaging objectives and seek simple solutions to the problem of motion design and control of a formation for imaging applications. Results indicate a tradeoff between image quality and fuel expenditure for the proposed class of maneuvers.

1 Introduction

The use of multiple spacecraft formations in interferometric imaging schemes gained much interest in recent years. The advantages such formations offer include the replacement of large monolithic telescopes and superior angular resolution. Order-of-magnitude advances in optical angular resolution via long baseline interferometry are sought for various NASA missions, such as the Origins program, and high resolution Earth imaging [1, 2].

The dynamics and control of spacecraft formations were given considerable attention in the past. For example, in [3, 4] spacecraft relative position dynamics are controlled for guaranteed closed-loop stability and in [5–7] decentralized controllers are proposed. In [8–11] control of spacecraft formation rotation is addressed. Fuel related problems were treated in [12, 13]. GPS utilization for spacecraft constellations is discussed in [14, 15]. Natural orbital dynamics were exploited for interferometric observatories [16, 17]. Controller design for formation keeping while in orbit where addressed in [18–20] and J_2 invariant orbits were sought in [21].

In the above studies, investigators assume prescribed motions that satisfy some imaging objective and seek to achieve these motions via active control. The question of which formation motions yield satisfactory imaging goals has not been addressed previously, with the exception of [17, 19]. In this paper we present a framework such that spacecraft motion planning and controller design meet desired imaging objectives.

2 Imaging Requirements

Interferometric imaging is performed by measuring the mutual intensity (the two point correlation [22]) that results from the collection and subsequent interference of two electric field measurements of a target made at two different observation points. While moving relative to

each other, the satellites collect and transmit these measurements, which are later combined at a central node using precise knowledge of their locations and timing of data collection. A least squares error estimate of the image can be reconstructed given the mutual intensity measurements, parameters of the optical system, and the physical configuration of the observatory.

Let \bar{z} be the distance from the image plane to the observation plane. By the term “picture frame” we denote the extent of the intended image on the image plane. The picture frame has a width \bar{L} . Pixelating the image plane into an $m \times m$ grid, the size of each pixel is $L = \bar{L}/m$, and the resulting angular resolution is $\theta_r = L/\bar{z}$. The angular extent of the desired picture frame is given by $\theta_p = \bar{L}/\bar{z}$, leading to $\theta_p = m\theta_r$.

To assess the quality of the reconstructed image, the reconstructed image is Fourier transformed into a two dimensional plane of spatial frequencies (the wave number plane.) At any given point on the wave number plane, the modulation transfer function (MTF) is defined as the ratio of the estimated intensity to the true image intensity. For an interferometric imaging constellation, the MTF can be computed given the measurement history and corresponding relative position data between the light collecting spacecraft. In the wave number plane, a point with a zero MTF value implies that the system is “blind” to the corresponding spatial frequency, while a large value of the MTF implies that the image signal can be restored at that wave number via an inverse Fourier transform [1, 22, 23]. The MTF, as a measure of the imaging system's performance, is a function of both the optical system and the configuration of the observatory in physical space. The MTF is related to the motion in physical space by [1]:

$$M(t, \vec{v}) = \int_0^t d\tau \sum_{i=1}^N \sum_{j=1}^N \hat{A}_p \left(\vec{v} - \frac{\vec{\chi}_i(\tau) - \vec{\chi}_j(\tau)}{\lambda} \right), \quad (1)$$

where N is the number of satellites in the formation, \vec{v} is the spatial wave number vector, $\vec{\chi}_i$ is the position vector of spacecraft i relative to a fixed frame, λ is the wavelength of interest and $\hat{A}_p(\vec{\zeta})$ is the Fourier transform of the picture frame function, $A_p(\vec{z})$, given by:

$$A_p(\vec{z}) = \begin{cases} 1 & \text{if } \vec{z} \in \text{desired picture frame} \\ 0 & \text{otherwise} \end{cases} \quad (2)$$

In this paper we address the issue of motion design and control for an interferometric observatory composed of two satellites that ensures a non-zero MTF within a desired region of the wave number plane. We assume that the system is in free space; the only forces acting on the

¹University of Michigan, ihussein@umich.edu

²University of Michigan, scheeres@umich.edu

³University of Michigan, dhiland@umich.edu

system are the spacecraft thrusters. One of the spacecraft is stationary and located at the origin of an inertial reference frame. Let $\mathbf{R}_1 \equiv \mathbf{0}$ and \mathbf{R}_2 be the position vectors of the first and second satellites, respectively. Thus \mathbf{R}_2 describes the relative position vector between the two satellites. Since we only consider the motion in a plane perpendicular to the line of sight of the formation, let \mathbf{r} be the projection of \mathbf{R}_2 onto such plane.

Dimensions of features in the wave number plane are the reciprocals of the corresponding dimensions in the physical plane. Thus, the resolution disc is a disc of diameter $\simeq 1/\theta_r$, and is the region where we desire a nonzero MTF (or, equivalently, wave number plane coverage.) The picture frame region is a circular disc of diameter $\simeq 1/\theta_p$. Therefore, the diameter of the resolution disc is m times the diameter of the picture frame disc in the wave number plane (see Figure (1).) As the relative position vector \mathbf{r} varies in the physical plane, the picture frame disc moves in the wave number plane, where its center follows the trajectory of the vectors given by $\pm\mathbf{r}/\lambda$, λ being the imaging wavelength of interest. Let $\tilde{\mathbf{r}} = \mathbf{r}/\lambda$. Each satellite, by itself, will contribute a disc that is centered at the origin with a diameter of $\simeq 1/\theta_p$, and each pair of satellites will contribute two discs of diameter $\simeq 1/\theta_p$ located 180 degrees apart with a radius of $\tilde{r} = \frac{r}{\lambda}$ from the center, where $r = |\mathbf{r}|$. In polar coordinates, r and \tilde{r} define the radial position of the second spacecraft in the physical plane and the picture frame disc centers in the wave number plane, respectively, and θ is the angular position of the spacecraft in the physical space and the first picture frame disc center, while the second (mirror image) picture frame disc center has an angular position of $\theta + \pi$.

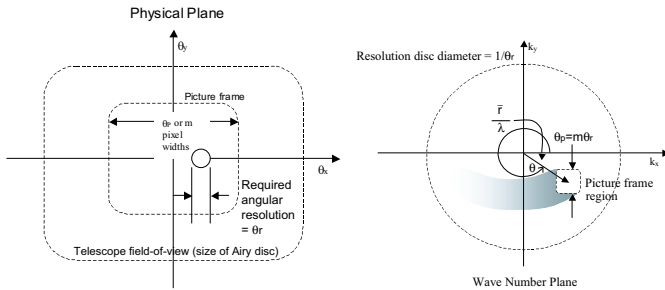


Figure 1: Physical and wave number plane variables.

3 Motion for Wave Number Plane Coverage

Here we only consider the motion of the second spacecraft (the first is fixed at the origin) and only one of the picture frame discs (while the second will have an identical motion that is symmetric about the origin.) Thus, by (\tilde{r}, θ) we imply the polar coordinates of one picture frame disc center. One way to ensure full coverage of the resolution disc is to initialize the second spacecraft such that at $t = 0$ we have $(\tilde{r} = \frac{1}{\theta_p}, \theta = 0)$,

make it follow a linear spiral as a function of θ , and to impose the terminal condition that at $t = t_f$ we have $(\tilde{r} = \frac{(m+1)}{2\theta_p}, \theta = \frac{(m-1)\pi}{2})$, where t_f is the terminal time. This motion implies that the two picture frame discs are initialized such that they lie outside the picture frame disc whose center is fixed at the origin, and moves spirally outwards till they lie outside the resolution disc.

Note that $\tilde{r} = 0$ is a singularity, which produces poor numerical results for the motion near the origin, and thus we do not initialize the system at this value. However, the discussion in Section 2 implies that initializing the system with $\tilde{r} = 1/\theta_p$ results in some regions close to the origin of the wave number plane that will not be covered (the shaded region in Figure (2).) It will be shown in simulation that this is not necessarily true, and that the initial condition we impose suffices for full coverage, especially near the origin. Thus \tilde{r} and θ are constrained to satisfy

$$\tilde{r}(\theta(t)) = \frac{1}{\pi\theta_p}(\pi + \theta), \quad \theta \in \left[0, \frac{(m-1)\pi}{2}\right]. \quad (3)$$

This implies that

$$r(\theta(t)) = \frac{\lambda}{\pi\theta_p}(\pi + \theta), \quad \theta \in \left[0, \frac{(m-1)\pi}{2}\right]. \quad (4)$$

The first and second time derivatives of the constraint (4) also need to be satisfied:

$$\dot{r} = \frac{\lambda}{\pi\theta_p}\dot{\theta}, \quad \text{and} \quad \ddot{r} = \frac{\lambda}{\pi\theta_p}\ddot{\theta}, \quad \forall t \in [0, t_f]. \quad (5)$$

Figure (2) shows an example of the trajectory in the physical and wave number planes for an object that is located at $\bar{z} = 15\text{pc}$ ($1\text{pc} = 3.085 \times 10^{13}\text{km}$), with a picture frame that is $\bar{L} = 12,760\text{km}$ wide, with $m = 17$ pixels and, thus, a pixel size of $L = 750.6\text{km}$ (i.e. this constellation maneuver is capable of detecting any object whose dimensions are larger than or equal to \bar{L} .) These are the values that are used throughout this paper. These values correspond to applications such as JPL's Terrestrial Planet Finder (TPF) and they could also be adjusted for Earth imaging applications. In the latter case, the maneuver spans a few meters only, as opposed to few thousands of kilometers as in the example we treat in this paper.

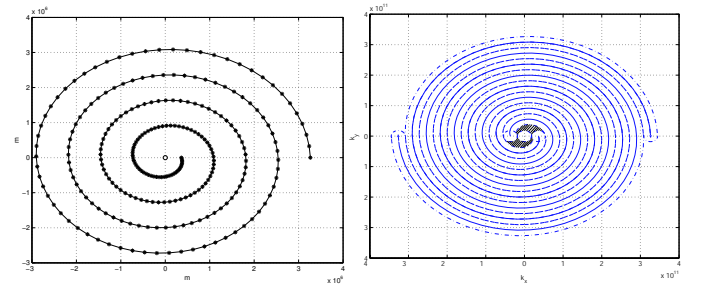


Figure 2: Motion in the physical (top) and wave number (bottom) planes.

4 Equations of Motion with a Spiral Constraint

In this section we derive the constrained equations of motion of the second spacecraft relative to the origin. After dividing throughout by the mass of the second spacecraft, the equations of motion for the system are described in polar coordinates by

$$\ddot{r} - r\dot{\theta}^2 = a_r, \quad (6)$$

and

$$r\ddot{\theta} + 2\dot{r}\dot{\theta} = a_t, \quad (7)$$

where a_r is the radial component of the thrust vector and a_t is the tangential component of the thrust vector, both divided by the mass of the spacecraft. Applying the configuration constraint in (4) to the system of equations (6)-(7) results in the following two *dependent* equations that describe the motion

$$\dot{\theta} - f(\theta)\dot{\theta}^2 = \tilde{a}_r, \quad (8)$$

and

$$f(\theta)\ddot{\theta} + 2\dot{\theta}^2 = \tilde{a}_t, \quad (9)$$

where $f(\theta) = \pi + \theta$, $\tilde{a}_r = \frac{\pi\theta_p}{\lambda}a_r$ and $\tilde{a}_t = \frac{\pi\theta_p}{\lambda}a_t$. Note that these two equations are equivalent. By solving for $\ddot{\theta}$ in (8) and (9) and equating the resulting expressions, one finds that the tangential and radial components of the force-per-mass vector are related such that

$$\tilde{a}_r = - \left[f(\theta) + \frac{2}{f(\theta)} \right] \dot{\theta}^2 + \frac{1}{f(\theta)} \tilde{a}_t. \quad (10)$$

By solving either (8) or (9) and (10) such that θ goes from 0 to $\frac{(m-1)\pi}{2}$ we are guaranteed that the spacecraft will have gone through one entire ‘‘image’’ maneuver and will have covered the wave number plane.

5 Simple Controllers to Achieve Imaging Objectives

In this section we investigate the performance of four controllers that are designed to satisfy the spiral motion constraint. The two main performance considerations are image quality and fuel consumption. Image quality requires full coverage of the resolution disc and the attainment of a desired signal-to-noise (S/N) ratio. An image quality performance measure can be expressed as:

$$\mathcal{I} = \int_0^{t_f} dt \int d\vec{v} (1 - \Gamma^R(\vec{v}, t)), \quad (11)$$

where R is a ‘‘risk factor’’ and $\Gamma(\vec{v}, t)$ is the estimated S/N ratio of the interferometric measurement divided by the desired S/N ratio. Using Poisson statistics in a semi-classical photon arrival fluctuation calculation (Section 4.4.3 in [24]), this can be shown to be proportional to the square root of the MTF magnitude:

$$\Gamma(\vec{v}, t) = \begin{cases} 1 & \text{if } \alpha M^{1/2} \geq 1 \\ \alpha M^{1/2} & \text{otherwise} \end{cases}, \quad (12)$$

where α is proportional to the desired S/N ratio and M is computed from Equation (1). The larger R is the more conservative the imaging performance measure becomes. Regions in the wave number plane where Γ is less than unity correspond to spatial frequencies of the signal that do not satisfy the desired S/N ratio. On the other hand,

$\Gamma = 1$ implies both coverage and achievement of the desired S/N ratio at the corresponding spatial frequency. $\Gamma = 1$ can be achieved if the relative speeds between the spacecraft in the constellation are less than or equal to a certain threshold value, denoted V_{SNR} . If the relative speed between any two spacecraft in the constellation is larger than V_{SNR} in some region of the wave number plane, the desired S/N ratio is not attained there.

In Section 2, we assume uniform sampling of the frequencies covered by the picture frame disc. The coverage it actually achieves has a nonuniform distribution that resembles a Gaussian. It can be shown that at low speeds the picture frame disc has an effective diameter that is larger than $1/\theta_p$ and for large speeds it will have one that is smaller than $1/\theta_p$. Thus, speed primarily affects S/N ratio and the effective width of the picture frame disc as it moves in the wave number plane.

The cost function used for fuel consumption is

$$\mathcal{U} = \int_0^{t_f} (a_r^2(t) + a_t^2(t)) dt. \quad (13)$$

The two cost functions in (11) and (13) are the basis for evaluating the imaging performance and fuel consumption. The sum $\mathcal{J} = w_1\mathcal{I} + w_2\mathcal{U}$, where w_i ($i = 1, 2$) are weighting coefficients, could be used as the objective function for a nonlinear optimal controller that optimizes both fuel consumption and image quality, which our group is currently investigating. Next we consider benchmark problems for controller design.

Maneuver 1: Constant Speed Motion As mentioned above, it is desirable to have a uniform S/N ratio over the entire resolution disc in the wave number plane. This can be achieved by setting the magnitude of the velocity to be:

$$V = \sqrt{(r\dot{\theta})^2 + \dot{r}^2} = V_{SNR}, \quad (14)$$

which is constant. Taking the derivative of this condition,

$$r\dot{\theta}(\dot{r}\dot{\theta} + r\ddot{\theta}) + \dot{r}\ddot{r} = 0,$$

substituting r , \dot{r} and \ddot{r} using (4)-(5) and rearranging one gets the closed loop differential equation

$$\ddot{\theta} = - \frac{f(\theta)}{1 + f^2(\theta)} \dot{\theta}^2, \quad (15)$$

which will achieve full coverage of the wave number plane if it satisfies the correct boundary conditions. From Equation (8), the radial component of the control thrust is given by

$$\tilde{a}_r = -f(\theta)\dot{\theta}^2 \left[1 + \frac{1}{1 + f^2(\theta)} \right]. \quad (16)$$

Using this and Equation (10), \tilde{a}_t is thus

$$\tilde{a}_t = \dot{\theta}^2 \left(2 - \frac{f^2(\theta)}{1 + f^2(\theta)} \right). \quad (17)$$

Maneuver 2: Constant Tangential Velocity A simplified version of the situation considered in the previous paragraph is to assume that only the tangential component of the velocity vector is constant; $V_t = r\dot{\theta}$ is

constant. Taking the the derivative of this condition,

$$\dot{r}\dot{\theta} + r\ddot{\theta} = 0, \quad (18)$$

substituting r , \dot{r} and \ddot{r} using (4)-(5) and rearranging one gets the closed loop differential equation

$$\ddot{\theta} = -\frac{1}{f(\theta)}\dot{\theta}^2. \quad (19)$$

From Equation (8), \tilde{a}_r is given by

$$\tilde{a}_r = -\dot{\theta}^2 \left[f(\theta) + \frac{1}{f(\theta)} \right]. \quad (20)$$

Using this and Equation (10), \tilde{a}_t is thus

$$\tilde{a}_t = \dot{\theta}^2. \quad (21)$$

Maneuver 3: Constant Angular Rate Next, consider the situation where $\dot{\theta}$ is a constant. Thus $\ddot{\theta} = 0$, which implies that θ is a linear function of time. After applying the boundary conditions, one obtains an explicit solution for θ

$$\theta(t) = \frac{(m-1)\pi}{2t_f}t. \quad (22)$$

Since $\dot{r} = \frac{\lambda}{\pi\theta_p}\dot{\theta}$, then $\ddot{r} = 0$. From Equations (8) and (9), \tilde{a}_r and \tilde{a}_t are given by

$$\tilde{a}_r = -f(\theta)\dot{\theta}^2 \text{ and } \tilde{a}_t = 2\dot{\theta}^2. \quad (23)$$

Maneuver 4: Zero Tangential Acceleration Consider not applying any tangential thrust; then $\tilde{a}_t = 0$ and Equation (10) implies that

$$\tilde{a}_r = \left[f(\theta) + \frac{2}{f(\theta)} \right] \dot{\theta}^2. \quad (24)$$

Finally, the closed loop differential equation is

$$\ddot{\theta} = -\frac{2}{f(\theta)}\dot{\theta}^2. \quad (25)$$

6 Results

In the results we present here, Maneuver (1) represents the benchmark solution to the problem. It is the solution that achieves the two imaging objectives since it follows a linear spiral that completely covers the desired resolution disc and it moves at a constant speed that is sufficient to attain the desired S/N ratio. First we determined the value of V_{SNR} and set the initial condition for Maneuver (1) such that the spacecraft has an initial speed equal to V_{SNR} , guaranteed to be maintained by the constraint (14). We simulated the system and determined the terminal time t_f , and for all other cases set the initial conditions such that each is completed at $t = t_f$. Finally, we use Equations (11) and (13) to evaluate the performance of all four motions. A reference speed, V_{SNR} , that achieves a desired S/N ratio of 150 was found to be 30m/s and t_f was found to be 17 days and 17 hours.

Figure (3) shows the time evolution of V for all four maneuvers. Figures (4) and (5) show how Γ accumulates and how the image forms with time for Maneuvers (1) and (4), respectively. These represent the two interesting cases: Maneuver (1) is the benchmark solution and Maneuver (4) shows that Γ by itself evaluated at the end of the maneuver is not sufficient to judge the quality of the final image. Maneuver (2) produces results almost

identical to Maneuver (1) and we will only comment on the results for Maneuver (3).

The image formation algorithm was developed by our group and has been used in this section to demonstrate the concepts presented in this paper. The algorithm assumes a given target planet, which includes planet surface details. It also assumes a statistical model for noise. It simulates the motion of the spacecraft, computes the resulting Γ function, and estimates the image.

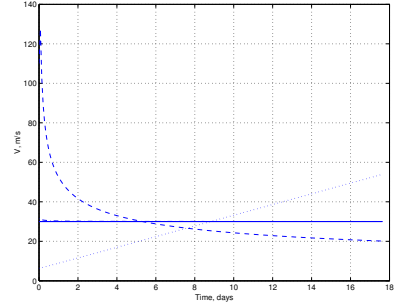


Figure 3: Total speed for Maneuver (1) (solid), Maneuver (2) (dash-dotted), Maneuver (3) (dotted) and Maneuver (4) (dashed).

For Maneuver (1), the speed is constant throughout the maneuver. This results in a uniform Γ function throughout the wave number plane (Figure (4)); the desired S/N ratio is attained everywhere in the plane. Maneuver (4), however, starts off with a speed of 110m/s, which is larger than V_{SNR} and a S/N ratio that is lower than the desired value is achieved near the center of the resolution disc. Thus, at low frequencies Maneuver (1) performs better than Maneuver (4).

As Maneuver (4) proceeds beyond the fifth day its speed drops below V_{SNR} , thus achieving the desired S/N ratio with a wider picture frame disc sample distribution. Beyond the fifth day of the maneuvers, both achieve equal imaging performance for all but the last 2π radians of the spiral. During the last spiral revolution, Maneuver (4) will have a wider picture frame disc than that of Maneuver (1) and will, thus, furnish bonus high frequency coverage in the wave number plane.

Therefore, during one phase Maneuver (1) has better imaging performance than Maneuver (4) but during the second phase the reverse statement is true. Figure (6) is a surface plot of the difference between the Γ functions of Maneuvers (1) and (4). As shown in Table (1), Maneuver (4) has an overall smaller imaging performance measure than Maneuver (1). This implies that the bonus coverage Maneuver (4) achieves at high frequencies outweighs its deficient coverage at low frequencies. If the imaging performance is restricted to the resolution disc only, then Maneuver (1) will achieve better imaging performance than Maneuver (4) because the latter leaves gaps at low frequencies.

Since the spacecraft in Maneuver (4) moves at a speed

lower than that in Maneuver (1), more fuel is required to slow it down. Indeed, Maneuver (4) is the least efficient maneuver as far as fuel consumption is concerned, but is the most efficient in terms of image quality.

Table (1) shows a summary of the performance of all four maneuvers. We note that Maneuvers (1) and (2) perform almost equally. Both result in intermediate image quality and fuel expenditure. Maneuver (3) requires the least amount of fuel but with the poorest imaging performance. The reverse statement is true for Maneuver (4). This result suggests that there exists a tradeoff between image quality and fuel expenditure.

Table 1: Performance measures for Maneuvers (1)-(4).

	$\mathcal{I}, \times 10^9$	\mathcal{U}
Maneuver (1)	5.14	0.53
Maneuver (2)	5.13	0.55
Maneuver (3)	6.27	0.46
Maneuver (4)	4.62	15.02

Finally, one may construct maneuvers by splitting the boundary value problem in θ into multiple boundary value problems with different controls over each segment. For example one can use the controller of Maneuver (3) and then switch to the controller of Maneuver (4) when the spacecraft's speed crosses 30m/s. This combined maneuver's performance is expected to have a lower fuel cost than Maneuver (4) but better imaging performance since \mathcal{I} will be accumulated over low speeds at both low and high frequencies.

7 Practical Considerations

Practical issues of concern include signal detection, transmission and interference. We assume that either a heterodyne or a direct detection method is used. Heterodyne detection has the advantage of selecting and detecting only components of the wavefront that are in phase with the wavefront of a local laser oscillator and, thus, furnishing phase information [25]. Though less efficient as far as S/N is concerned, direct detection is feasible via spatial filtering to obtain a single geometric mode [26]. The major advantage of using local heterodyne detection over using a direct detection technique is that with more than two satellites, the latter requires that the detected signal be divided into $N - 1$ equal parts, where N is the number of satellites in the constellation, corresponding to $N - 1$ baselines. This results in the reduction of the signal by a factor of $N - 1$. Each of the $N - 1$ signals will possess a reduced S/N ratio. This is exacerbated due to the presence of large background noise and the long distances over which the signals are transmitted from each spacecraft to a combiner spacecraft. For wavelengths above $\sim 4\mu\text{m}$, heterodyne detection is likely to be superior because of these problems with direct detection. It could be shown, how-

ever, that below $\sim 4\mu\text{m}$ direct detection will have better S/N properties than heterodyne detection. For a $10\mu\text{m}$ mission, heterodyne detection is advantageous.

Alternatively, one may consider Fourier Transform Spectral Interferometry for electric field reconstruction in a separated spacecraft interferometric mission. Novel optical techniques, such as Dual-Quadrature Spectral Interferometry (DQSI) and Spectral Phase Interferometry for Direct Electric Field Reconstruction (SPIDER), aim at full temporal and spatial characterization of an electric field [27, 28]. The goal of such methods, which has so far been developed for highly coherent sources and is currently being developed for non-coherent sources, is to extract necessary information in digital form that allow for performing the interference process digitally on a microchip. Once such digital information is available these can be sent via (radio frequency) communication links to a central processing unit located on one of the spacecraft for mutual intensity computations and metrology measurements. In light of technologies such as heterodyne detection or electric field reconstruction, a very long baseline mission such as the one we propose in this paper should be feasible.

8 Current and Future Work

In this paper we have introduced some basic notions that relate the imaging problem to the motion and controller design problem. Results show evidence of a tradeoff between image quality and fuel expenditure. Currently, our research is focused on computing an optimal controller that optimizes over fuel consumption and image quality. Future research will investigate the effects of a general gravitational field on the solution and will seek the exploitation of this field to reduce fuel consumption of such a spiral maneuver. Other classes of formation maneuvers, possibly with a larger number of satellites, will be sought to achieve the desired imaging goals we discussed in this paper.

References

- [1] Hyland, D. C. Interferometric Imaging Concepts With Reduced Formation-Keeping Constraints. *AIAA Space Conf.*, Albuquerque, NM, August, 2001.
- [2] Gano, S. et. al. A Baseline Study of a Low-Cost, High-Resolution, Imaging System Using Wavefront Reconstruction. *AIAA Space Conf.*, Albuquerque, NM, August, 2001.
- [3] Kapila, V. et. al. *ACC Proc.*, 4137-4141, June 1999.
- [4] Marcio, S. et. al. *J. Guidance, Control, and Dynamics*, V. 23, No. 3, 385-390, May-June 2000.
- [5] Carpenter, J. R. *IEEE Aero. Conf. Proc.*, V. 7, 63-74, 2000.
- [6] Lawton, J. et. al. *Proc. IEEE Int. Conf. on Robotics and Automation*, Vol. 3, 2728-2733, 2000.
- [7] Kang, W. et. al. *J. of Guidance, Control and Dynamics*, Vol. 24, No. 2, 360-368, March-April 2001.
- [8] Lawton, J. et. al. *ACC Proc.*, 1545-1549, June 1999.

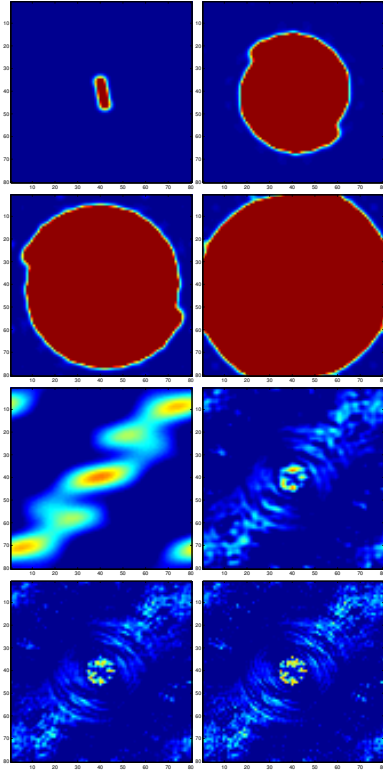


Figure 4: Γ (top four figures) and estimated image (bottom four figures) at $t = 0$, at $t = 5.9$ days, at $t = 11.8$ days and at $t = 17.7$ days for Maneuver (1).

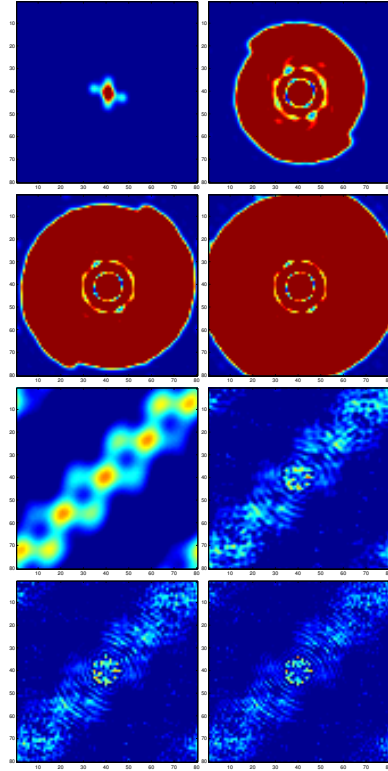


Figure 5: Γ (top four figures) and estimated image (bottom four figures) at $t = 0$, at $t = 5.9$ days, at $t = 11.8$ days and at $t = 17.7$ days for Maneuver (4).

- [9] Wang, P. and J. Yee. *J. of Guidance, Control, and Dynamics*, Vol. 24, No. 2, 352-359, March-April 2001.
- [10] Wang, P. et. al. *J. of Guidance, Control, and Dynamics*, Vol. 22, No. 1, 28-35, January-February 1999.
- [11] Beard, R. and F. Hadaegh. *ACC Proc.*, 4383-4387, June 1999.
- [12] Beard, R. and F. Hadaegh. *ACC Proc.*, 2975-2979, June 1999.
- [13] Beard, R. et. al. *ACC Proc.*, 1580-1584, June 1998.
- [14] Robertson, A. et. al. *ACC Proc.*, 1574-1579, June 1998.
- [15] Lau, K. et. al. *Guidance, Navigation and Control Conf.*, 3819-3828, July 1996.
- [16] Kong, E. et. al. *ACC Proc.*, 4153-4157, June 1999.
- [17] Hussein, I. et. al. *Interferometric Observatories in Earth Orbit, 2003 AAS/AIAA Space Flight Mechanics Meeting*, Ponce, Puerto Rico, February 9-13, 2003.
- [18] Vassar, R. and R. Sherwood. *J. of Guidance*, V. 8, No. 2, 235-242, 1985.
- [19] DeCou, A. *J. of the Astronautical Sciences*, V. 39, No. 3, 283-297, July-September 1991.
- [20] Schaub, H. et. al. *J. of the Astronautical Sciences*, V. 48, No. 1, 69-87, 2000.
- [21] Schaub, H. and K. Alfriend. *Celestial Mechanics and Dynamical Astronomy*, V. 79, 77-95, 2001.
- [22] Born, M. and E. Wolf. *Principles of optics*, Pergamon Press, New York, 1964.

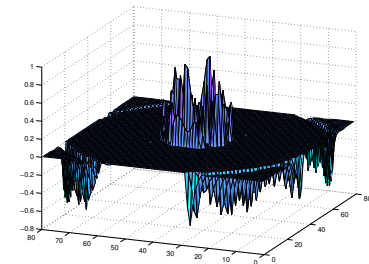


Figure 6: $\Gamma_1 - \Gamma_4$.

- [23] Hyland, D. C. The Inverse Huygens-Fresnel Principle and Its Implications for Interferometric Imaging. *Journal of the Astronautical Sciences*, to appear.
- [24] Mandel, L. and E. Wolf. *Optical Coherence and Quantum Optics*. Cambridge University Press, 1995.
- [25] Townes, H. Ch. 4 of *Principles of Long Baseline Interferometry*. Michelson Summer School Course Notes, Aug. 15-19, 1999, P. Lawson, Ed. JPL Publication 00-009, July 2000.
- [26] Kingston, R. *J. Opt. Soc. Am. B.*, V. 4, 1450-1741, 1978.
- [27] Lepetit, L. et. al. *J. Opt. Soc. Am. B*, V. 12, No. 12, 1995.
- [28] Iaconis, C. and I. Walmsley. *IEEE J. of Quantum Mechanics*, V. 35, No. 4, 1999.